NANO LETTERS
pubs.acs.org/NanoLett
Letter

Nanoscale Magnetization and Current Imaging Using Time-Resolved Scanning-Probe Magnetothermal Microscopy

Chi Zhang, Jason M. Bartell, Jonathan C. Karsch, Isaiah Gray, and Gregory D. Fuchs*

Cite This: *Nano Lett.* 2021, 21, 4966−4972

Read Online

ACCESS | Metrics & More | Article Recommendations | SI Supporting Information

ABSTRACT: Magnetic microscopy that combines nanoscale spatial resolution with picosecond scale temporal resolution uniquely enables direct observation of the spatiotemporal magnetic phenomena that are relevant to future high-speed, high-density magnetic storage and logic technologies. Magnetic microscopes that combine these metrics has been limited to facility-level instruments. To address this gap in lab-accessible spatiotemporal imaging, we develop a time-resolved near-field magnetic microscope based on magnetothermal interactions. We demonstrate both magnetization and current density imaging modalities, each with spatial resolution that far surpasses the optical diffraction limit. In addition, we study the near-field and time-resolved characteristics of our signal and find that our instrument possesses a spatial resolution on the scale of 100 nm and a temporal resolution below 100 ps. Our results demonstrate an accessible and comparatively low-cost approach to nanoscale spatiotemporal magnetic microscopy in a table-top form to aid the science and technology of dynamic magnetic devices with complex spin textures.

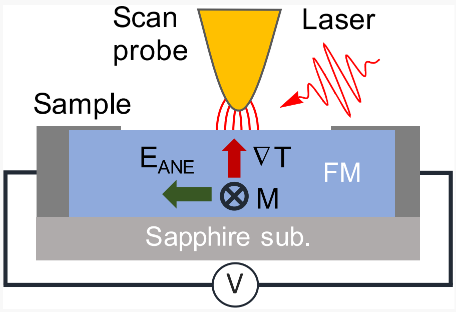

KEYWORDS: *magnetic imaging, scanning probe microscopy, near-field microscopy, magnetothermal effects, spatiotemporal*

Advanced magnetic microscopies are a key tool for advancing our understanding of novel magnetic phenomena, such as skyrmions, spin waves, and domain walls.[1−3] Imaging these phenomena increasingly requires 10−100 nm spatial resolution[1,4−7] 10−100 ps temporal resolution.[8,9] Simultaneously achieving both resolutions enables the study of both static and dynamic nanoscale magnetic textures that are interesting for high-performance technology, such as skyrmion dynamics and spin torque oscillators.[10−12] Unfortunately, most magnetic microscopies offer either nanoscale spatial resolution or picosecond temporal resolution, but not both. The techniques with both of these characteristics include X-ray based microscopes,[13] which require a synchrotron facility, and time-resolved electron microscopes,[14,15] which are expensive and not widely available. No low-cost and widely accessible tabletop techniques currently exist.

To break free of the optical diffraction limit while retaining the stroboscopic imaging capabilities offered by pulsed lasers, our approach is to use picosecond thermal pulses generated by a near-field probe-sample interaction. Recently, we have demonstrated time-resolved magnetothermal microscopy, with picosecond temporal resolution and spatial resolution determined by focused light.[16−18] In this technique, a focused light pulse generates a microscale thermal gradient. Through the anomalous Nernst effect, the local magnetization is transduced into a voltage. This approach has proven to be useful for imaging both local static and dynamic magnetization,[16] as well as an applied current density.[18] It has also been applied to a wide range of materials beyond magnetic metals, such as magnetic insulators[17] and antiferromagnets[16,19−22] using the longitudinal spin Seebeck effect. The spatial resolution of time-resolved magnetothermal microscopy can be further extended to the nanoscale using a scanning probe for near-field excitation. We note a parallel work to ours uses near-field magnetothermal effects in a similar way with a continuous wave thermal gradient for detecting static magnetizations.[22,23]

Here, we demonstrate the spatiotemporal near-field magnetothermal microscope for magnetization and applied current density imaging. We confirm the near-field character of the signal by its probe-sample distance dependence. By imaging current density around a nanoconstriction that provides a well-controlled nanoscale feature, we demonstrate 100 nm-scale spatial resolution. We also verify the stroboscopic capabilities of the microscope by directly measuring a gigahertz frequency current density as a function of oscillation phase. These results provide a table-top solution to nanoscale spatiotemporal magnetic microscopy aimed at emerging complex nanoscale magnetic phenomena.

Received: February 19, 2021
Revised: June 2, 2021
Published: June 8, 2021

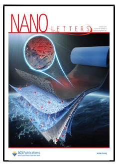

We introduce the operating principles of our scanning near-field magnetothermal microscope. We first discuss the principles of magnetothermal microscopy (Figure 1a) based on measuring thermally induced electric fields described by

$$\mathbf{E}_{\mathrm{ANE}}(\mathbf{x}, t) + \mathbf{E}_J(\mathbf{x}, t) = -N\mathbf{m}(\mathbf{x}, t) \times \nabla T(\mathbf{x}, t) + \mathbf{J}(\mathbf{x}, t)\Delta\rho(\Delta T, \mathbf{x}, t) \quad (1)$$

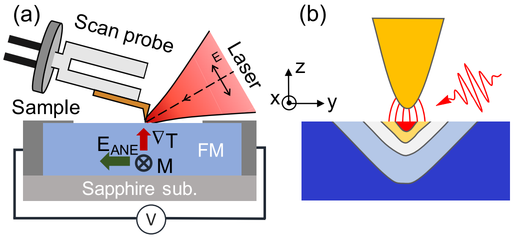

Figure 1. Experimental schematics. (a) Schematic of the scanning near-field magnetothermal microscope illustrating the configuration of the scan probe, the laser, and the anomalous Nernst effect (ANE) in the ferromagnetic (FM) sample. The thermal excitation ∇T (ΔT) generated by the near-field tip is used to probe local magnetization $\boldsymbol{m}$ (applied current density $\boldsymbol{J}$). (b) Near-field enhancement of the electric field generated by an optical pulse locally heats the sample in a region with size comparable to the radius of tip apex. The colors on the sample represent contours of temperature increase due to near-field heating as discussed in ref 24.

To experimentally access these effects, we apply a pulsed laser, either directly focused or nanoconfined by the near-field tip, to create a transient local temperature increase, ΔT, and a corresponding local gradient ∇T. The local magnetization $\boldsymbol{m}$ subjected to ∇T generates an electric field $\boldsymbol{E}_{\mathrm{ANE}}$ through the anomalous Nernst effect (ANE),[25−38] with coefficient N. On the basis of the prior finite-element modeling for our materials and configuration, the vertical component of the thermal gradient dominates over the lateral component of the thermal gradient.[24] In addition, throughout this paper, we study in-plane magnetized samples. Therefore, the device ANE voltage produced from the local $\boldsymbol{E}_{\mathrm{ANE}}$ is proportional to the in-plane component of the magnetization perpendicular to the voltage contacts within the thermally excited region. In Figure 1a, since the contacts are along y, we measure the m_x component of the magnetization. The second term of eq 1 provides an extension of this technique to image current density. $\boldsymbol{E}_J$ arises from a current density $\boldsymbol{J}$ passing through the thermally excited sample volume with locally increased resistivity $\Delta\rho$. Ohm's law requires an extra electric field $\boldsymbol{E}_J = \boldsymbol{J}\Delta\rho$, which is time-dependent due to the picosecond transience of laser heating of thin metal films.[18] These two signals combine to form a voltage pulse train that we amplify and subsequently demodulate by mixing with an electrical reference pulse train.[16,18]

For the scanning probe, we use a tuning fork-based atomic force microscope (AFM) in tapping mode. We use probe frequency feedback to maintain an average probe-sample separation. The probe is a gold-coated Si cantilever glued to a tuning fork. The tip radius is 30 nm as received, which gets broader with scanning and reaches 50 nm or more by the time we complete the alignment procedure and record data. The probe oscillates at the tuning fork resonance frequency $f = 32$ kHz with a typical amplitude of 40 nm. We illuminate the tip apex with laser pulses (p-polarized, angle of incidence 30°, laser fluence 1 mJ/cm^2 with a 76 MHz repetition rate) from a Ti:sapphire laser (3 ps-wide, wavelength $\lambda = 785$ nm), focused using a microscope objective (numerical aperture NA = 0.42). The near-field interaction enhances the electric field in a region confined at the tip apex[39−42] (Figure 1b). This electric field heats the sample in a manner similar to that of the focused laser, now used as a nanoscale heat source. The resultant heating profile is confined to an area comparable to the tip radius, below 100 nm.[24] We note that the near-field optical heating is also the basis for heat-assisted magnetic recording (HAMR) technology.[43−46] In the measurement, the light falls onto both the sample and the tip. The focused light and the scanning probe near-field excitation both generate thermal profiles that induce "far-field" and "near-field" signals, respectively. We separate these contributions using lock-in detection. To recover the far-field signal, we demodulate at the 2 kHz frequency of the laser chopper. To recover the near-field signal, we use the fact that near-field interactions drop off exponentially with increasing tip−sample distance on the order of the tip radius.[40] As the probe oscillates, this nonlinearity creates a modulation at the probe frequency and harmonics (2*f*, 3*f*, etc.). We throughout the paper demodulate the near-field signal at the second harmonic of the probe frequency. Because some far-field light can be reflected or shadowed by tip probe motion, the first harmonic contains a mixture of near- and far-field signals. The far-field contributions are linear, however, and thus they are largely suppressed in the 2*f* demodulation channel.[40,47,48]

First, we demonstrate that a scanning near-field magnetothermal probe can detect local magnetization and current density. We study a 5 μm × 12 μm CoFeB (4 nm)/Hf (2 nm)/Pt (4 nm) sample fabricated using photolithography.[18] To align the tip and sample, we first scan the sample (on a scanning *xy* stage) using topography in standard AFM mode. Then, with the tip retracted, we align the laser to the same features on the sample using the far-field magnetothermal signal as in a conventional magnetothermal microscope except here with a 30° incident angle. This process coarsely aligns the laser with the tip. We, then, approach the tip to the surface and adjust the laser position to maximize the near-field signal.

In Figure 2a, we show the near-field imaging of a uniform magnetic state. We apply a saturating 50 Oe magnetic field perpendicular to the channel and measure near-field line scans across the sample width as depicted in the schematic in Figure 2b. The near-field signal changes sign with magnetization direction, which demonstrates that we sense magnetic orientation. We note that the signal crosses zero and then decays at the sample edges rather than approaching zero sharply. This is because there are some artifact signals getting into the 2*f* demodulation channel. The amount of artifact varies from tip to tip, and could depend on tip sharpness and the slight misalignment between the laser and tip. In Figure 2b, we apply DC current through the sample to measure near-field line cuts of current density. With the application of a 1.5 mA current, in addition to a ~1 μV uniform remnant state magnetic signal at zero field (eq 1), the contribution from current density dominates the total signal. The near-field signal changes sign with current polarity, which confirms that the signal is sensitive to current density.

Next, we demonstrate magnetic imaging of a multidomain state. We demagnetize the sample using a series of minor loops with reducing field extent. First, imaging without the tip, Figure 2c shows a focused-light far-field image demodulated with respect to the optical chopper that shows magnetic domains in

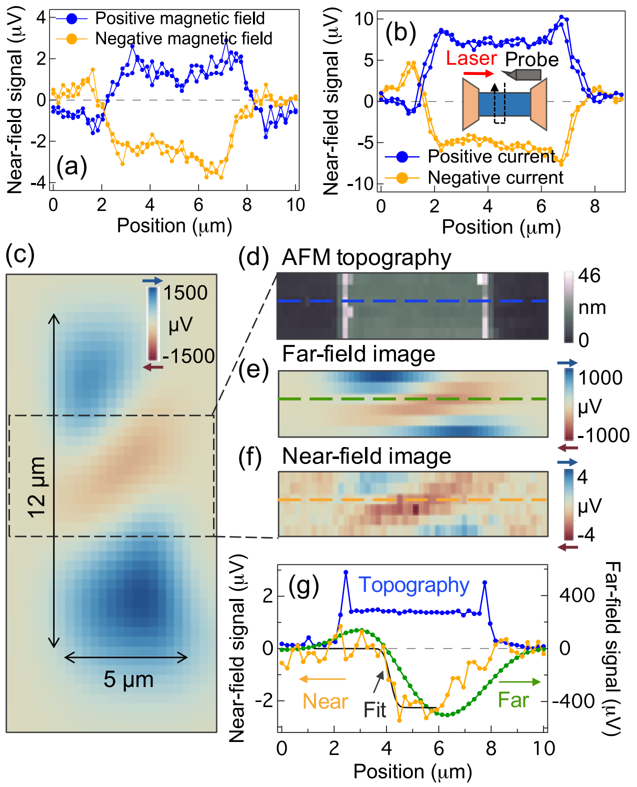

Figure 2. Line scans and magnetic multidomain imaging. Near-field line scans across the sample width at opposite (a) magnetization orientations and (b) applied current polarity. Panels a and b show forward and backward line traces indicated by the inset in panel b. (c) Magnetic far-field images of a multidomain state without a scanning probe tip. (d−f) Images and (g) representative line cuts of topography, far-field, and near-field images acquired with the scanning probe. In panels c, e, and f, the blue and red contrast show local magnetization pointing right and left, respectively. Panel e is acquired after panel f with the tip retracted for a tip-unperturbed far-field image for comparison, using the same scan parameters as in panel f: the scan area is 10 μm × 6 μm, and we use a lock-in time constant of 1 s. The dashed lines in panels d−f indicate the line cuts in panel g.

a wide field-of-view at zero magnetic field in low resolution. Corresponding to the dashed region shown in Figure 2c, Figure 2d−g shows images and representative line cuts of tuning fork-AFM topography, the chopper referenced far-field signal, and the probe referenced near-field signal, acquired with the scanning probe. We see that the near-field image agrees well with the known far-field domain image but has higher resolution. To estimate the characteristic length of the near-field features, we fit a linecut across the domain wall to $\frac{C}{2}\left(1 + \text{erf}\left(\frac{x - x_0}{\sqrt{2}\,\delta}\right)\right)$, with the full-width at half-maximum (fwhm) of the curve given by $2\sqrt{2\ln 2}\,\delta$. The fit shown in Figure 2g yields a width of 455 nm even at a 37° angle with the domain wall direction, which is below the optical diffraction limit of the setup, approximately $\lambda/(2\ \text{NA}) = 1402$ nm (NA = 0.28 used for Figure 2c−g only). This width is consistent with the expected domain wall width in this material due to its low anisotropy.[49−51] Therefore, this measurement does not reveal the instrument resolution. We further characterize instrument resolution in subsequent measurements.

Here, we discuss the sensitivity of the near-field scanning probe for magnetic and current signals. The magnetization angle sensitivity is estimated[16] to be $\theta_{\min} = 4.9°/\sqrt{\text{Hz}}$ for a 5 μm-width CoFeB sample. This is less sensitive than we have achieved with the conventional focused light magnetothermal setup, however, we note that the sensitivity is dependent on several factors including the sample impedance, the Nernst coefficient, and the sample width. The signal scales inversely with the sample width due to the effective resistance shunting, and therefore the near-field scanning probe is most suitable for studying samples ≤1 μm wide. We estimate the current density sensitivity to be $3.57 \times 10^9\,\text{A}/(\text{m}^2\sqrt{\text{Hz}})$ for a 5 μm-width sample. The current density signal again scales inversely with the sample width, and thus, we obtain better sensitivity in the narrower-width devices discussed in subsequent measurements.

We examine how the signal depends on tip−sample separation to study the origin of our signals. Near-field interactions are only non-negligible when the tip is at short distances from the sample, on the order of tip radius.[40] We measure both magnetic and current signals collected from the probe-demodulated lock-in as we bring the dynamically tapping tip close to the sample. In our configuration, the laser is prealigned to the sample when the tip is approached, and the tip−sample displacement is controlled by retracting or approaching the tip. A near-field contribution drops off over nanoscale distances, while a far-field contribution drops off with microscale displacements corresponding to the laser intensity distribution.[47] We simultaneously measure the near-field signals as well as probe parameters for tip-height characterization. Figure 3 shows that the near-field signals increase when the tip is in first contact with the sample, indictated by an initial increase of the frequency and decrease of the amplitude. The 100 nm short-range increase of the signal is consistent with the near-field interaction.[40] In addition, Figure 3a shows that the far-field artifact is largely suppressed with demodulation of the signal at 2*f*.

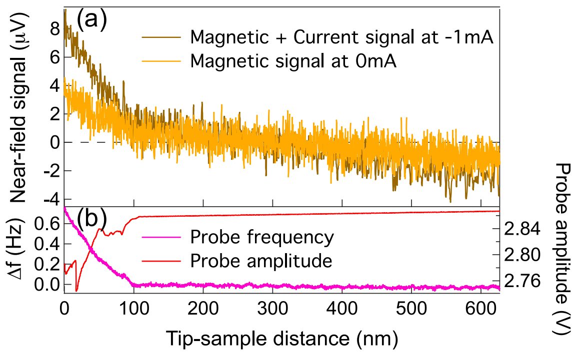

Figure 3. Near-field characteristic. Tip−sample distance dependence of (a) near-field signals and (b) probe parameters (probe frequency and amplitude).

We further characterize the spatial resolution of the instrument. Here, we measure in current imaging mode, and design a new sample with narrow constrictions that confine the current density in a width comparable to the tip dimension. The sample is a $\text{Ni}_{80}\text{Fe}_{20}$ (5 nm)/Ru (2 nm) film, fabricated using e-beam lithography into a 2 μm-diameter disk with two 150 nm wide necks (Figure 4a inset). Figure 4a and b shows topography and near-field current density images taken with the near-field scanning probe, at an applied current of −0.03 mA. We see that the current density is indeed concentrated at

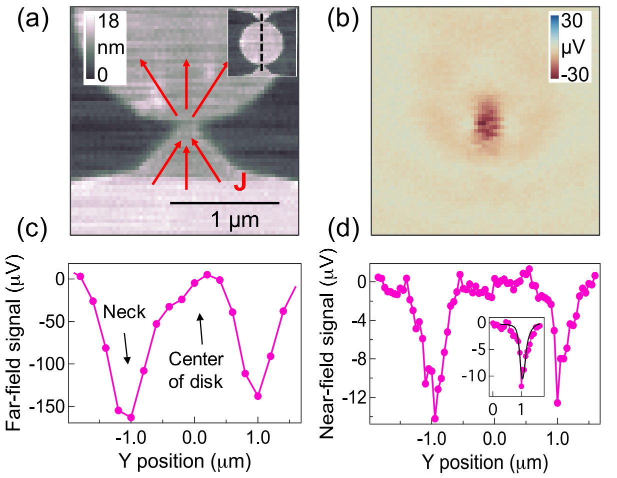

Figure 4. Current imaging and spatial resolution. (a) Topography and (b) current density images acquired by a near-field tip. The inset of (a) is a wider field of view. The scan area on the sample is 2 μm × 2 μm and we use a lock-in time constant of 200 ms (30 min image acquisition time). Line scans through two necks (as illustrated by the dashed line in the inset of panel a) of (c) far-field and (d) near-field signals for resolution comparison. Panel d is scanned in the y direction, taken separately from the image in panel b with the slow-scan axis along x. Since the sample geometry is asymmetric around the neck, we expect the peak to be asymmetric, which is seen in the near-field signal. (d) Inset: Pure current density contribution obtained by computing the half difference of data acquired for positive and negative currents. The line is a fit to the data with width δ = 74 nm. Details of the fit are given in the Supporting Information.

the neck. By measuring line scans through two necks (Figure 4a inset), we compare signals between focused light far-field (Figure 4c) and scanning probe near-field (Figure 4d) microscopy. In Figure 4c, we measure this sample in our conventional magnetothermal microscope[16−18] that uses directly focused light (angle of incidence 90°, numerical aperture of 0.9). By fitting the peak with a Gaussian function, the extracted fwhm resolution of 740 nm is consistent with the focused light setup resolution.[16]

We quantitatively extract spatial resolution from Figure 4(d), based on a sharp feature in the line scan (the right side peak). We simulate the current density distribution around the neck using COMSOL (see supplement), and convolve it with a Gaussian point spread function, converted to voltage. We fit the simulated result to our data, with a Gaussian width δ as the fitting parameter. The representative fit gives δ = 74 nm (corresponding to a fwhm of 165 nm). This resolution is less than 1/4 of our focused light magnetothermal microscopy resolution with highest NA,[16] which is consistent with the subdiffraction resolution of near-field microscopy. We note that the experimentally extracted value is for current imaging (determined by temperature increase ΔT), not a magnetic measurement (determined by thermal gradient ∇T).[16,18,24] A magnetic spatial resolution is likely higher than current,[16] therefore below the extracted value. In previous work,[24] finite-element simulations showed that the fwhm resolution of magnetic imaging using a near-field tip is approximately the tip diameter.[24] On the basis of this analysis, we estimate the tip radius when we take the data to be 65 nm, which is consistent with the scanning electron microscope image of the tip taken after the measurements. We note that the resolution, here, is only an upper bound and that it depends on the tip sharpness at the time of scanning. We expect a fwhm resolution of 50 nm using magnetothermal microscopy with sharp, high-endurance tips.[24]

Now, we turn our attention to characterizing temporal resolution of our instrument. We use 3 ps laser pulses to create thermal excitations, and thus, the temporal resolution of magnetization (current density) measurement is determined by the temporal width of the generated thermal gradient ∇T (temperature increase ΔT).[16] In prior work using focused light magnetothermal microscopy, finite-element simulation showed that the thermal gradient pulse has a width of ∼10 ps, and experiments verified an upper bound of 30 ps.[16] For thermal gradients generated by a near-field tip, the finite-element simulation gave a temporal width within 6 ps.[24] Therefore, whether the excitation is from a far-field or near-field source, the picosecond-scale temporal resolution are expected to be similar. Here, we experimentally examine the stroboscopic temporal properties of near-field magnetothermal microscopy.

Figure 5a and b show a measurement of the picosecond-scale voltage pulses that are directly created in response to a transient ΔT or ∇T in the presence of an applied current density or a static magnetization.[16] The short-lived thermal excitation of the sample is the origin of the stroboscopic time dependence of magnetothermal microscopy. We measure the pulses by combining them in an electrical mixer with 100 ps electrical reference pulses that are synchronized with the laser but have a controllable delay τ.[16,18] Figure 5a and b show the mixed output voltage as a function of the delay τ, which can be

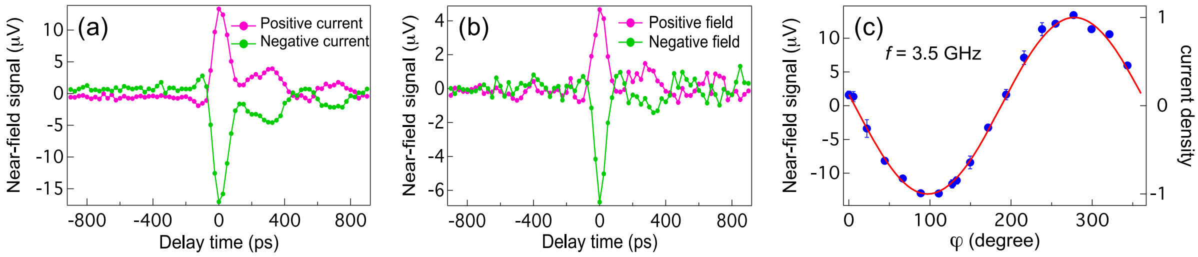

Figure 5. Stroboscopic measurements of microwave current. Time-domain measurements of the near-field voltage pulses produced by (a) current density (measured at the neck of the $\mathrm{Ni_{80}Fe_{20}}$ sample) and (b) magnetization (measured at the center of the CoFeB sample) as a function of the pulse delay τ between the voltage pulses generated at the sample and the 100 ps-width square reference pulses. A pulse delay of zero corresponds to the two pulse trains entering the mixer at the same time. The feature that follows the main peak is due to electrical reflections in the detection circuits[16,17] (c) Normalized microwave current density at the neck of $\mathrm{Ni_{80}Fe_{20}}$ sample measured as a function of φ stroboscopically probed by the thermal pulses. The red curve is a sinusoidal fit. The near-field signal is vertically offset to subtract the static magnetic signal contribution, obtained from the sinusoidal fitting.

understood as the temporal convolution signal of the voltage pulses with the reference pulses.[16] In both plots, the convolved signal widths are roughly 100 ps, similar to the reference pulse width. Therefore, the voltage pulses generated by the near-field thermal excitations must be shorter than 100 ps, demonstrating a time-resolved nanoprobe.

In Figure 5c, we also demonstrate a stroboscopic capability of the scanning probe to measure current density with temporal resolution that exceeds one-half[16] the oscillation period of a 3.5 GHz current applied directly to our device. To make this measurement, we synchronize the laser and microwave current by choosing a frequency at an integer multiple of the laser repetition rate such that the thermal pulses constantly probe the current at the same phase, φ.[16,18] Here, φ is a relative phase between the microwave current and the laser with a phase offset that depends on frequency and initial conditions. Time-resolved measurements of current imply that we can use our near-field microscope to make phase-sensitive observations of microwave current within a nanoscopic volume. Figure 5c shows normalized microwave current density as a function of φ, showing the phase-sensitive response. As we rotate φ, we observe the expected sinusoidal response in the near-field signal.

In conclusion, we demonstrate scanning near-field magnetothermal microscopy of magnetization and current density using picosecond thermal pulses. This work represents an important milestone for low-cost, table-top magnetic microscopy that unifies nanoscale spatial resolution with picosecond temporal resolution in the same instrument. Here, we experimentally image magnetic domains with nanoscale resolution, and we verify the near-field origin of both magnetic and current density contrast with a spatial resolution on the scale of 100 nm. Additionally, we demonstrate picosecond-scale temporal resolution of current density and magnetization, enabling a stroboscopic nanoscale probe of emerging magnetic devices in which we can directly probe both a stimulus and its response. For example, nanoscale phase-sensitive imaging could be useful for understanding mechanisms and phase-relationships in mutual synchronization locking of spin−orbit torque oscillators.[12] Meanwhile, the capability to image current from DC to microwave frequencies could clarify the origins of magnetic resonances in spatially nonuniform spin-Hall nanodevices.[52]

We are optimistic that scanning probe magnetothermal microscopy can be further developed into a powerful tool to study the dynamics of nanoscale magnetic devices and spin textures,[53,54] a capability that time-resolved scanning near-field probe uniquely provides as compared to CW magnetothermal microscopy.[22,27,55] For example, the spatial and temporal resolution of our microscopy is compatible with measuring magnetic resonance from a single magnetic skyrmion, rather than from an ensemble.[10] Furthermore, magnetothermal microscopy is compatible with a wide palette of magnetic materials beyond magnetic metals, including ferrimagnetic magnetic insulators[17] and antiferromagnetic insulators[19] (via the spin Seebeck effect, with an electrical channel provided, for example, by an interfacial Pt layer), thus offering a versatile imaging tool. Scanning probe magnetothermal microscopy is especially suitable for devices with submicron channel widths and using materials that have strong magnetothermal effects. Indeed, improving the sensitivity of this instrument will be the most important step forward in its future development. The magnetization sensitivity can be further improved through optimization of the instrument (e.g., detection electronics, impedance matching, probe amplitude optimization,[40] tip sharpness) and through incorporation of near-field engineering (including a plasmonic coupling grating[47,56−59]).

■ ASSOCIATED CONTENT

Supporting Information

The Supporting Information is available free of charge at https://pubs.acs.org/doi/10.1021/acs.nanolett.1c00704.

> Further details on optical and electrical setup; further analysis of magnetic feature size and sensitivity; current density distribution, spatial resolution extraction, and further discussion on spatiotemporal profiles of thermal excitations; and tip alignment and tip artifact (PDF)

■ AUTHOR INFORMATION

Corresponding Author

Gregory D. Fuchs − *School of Applied and Engineering Physics, Cornell University, Ithaca, New York 14853, United States;* orcid.org/0000-0003-4343-8523; Email: gdf9@cornell.edu

Authors

Chi Zhang − *School of Applied and Engineering Physics, Cornell University, Ithaca, New York 14853, United States*
Jason M. Bartell − *School of Applied and Engineering Physics, Cornell University, Ithaca, New York 14853, United States*
Jonathan C. Karsch − *School of Applied and Engineering Physics, Cornell University, Ithaca, New York 14853, United States;* Present Address: Pritzker School of Molecular Engineering, University of Chicago, Chicago, Illinois 60637, United States
Isaiah Gray − *School of Applied and Engineering Physics, Cornell University, Ithaca, New York 14853, United States*

Complete contact information is available at: https://pubs.acs.org/10.1021/acs.nanolett.1c00704

Notes

The authors declare no competing financial interest.

■ ACKNOWLEDGMENTS

We thank Dr. Long Ju, Dr. Samuel Berweger, and Harry Cheung for helpful discussions. Time-resolved and current imaging studies were supported by the DOE Office of Science, Basic Energy Sciences (DE-SC0019997). Preliminary development and static magnetic imaging was supported by the AFOSR (FA9550-14-1-0243, FA9550-18-1-0408). This work made use of the Cornell Center for Materials Research Shared Facilities, which are supported through the NSF MRSEC program (DMR-1719875), and the Cornell NanoScale Facility, a member of the National Nanotechnology Coordinated Infrastructure (NNCI), which is supported by the National Science Foundation (Grant NNCI-2025233).

■ REFERENCES

(1) Yu, X. Z.; Onose, Y.; Kanazawa, N.; Park, J. H.; Han, J. H.; Matsui, Y.; Nagaosa, N.; Tokura, Y. Real-space observation of a two-dimensional skyrmion crystal. *Nature (London, U. K.)* **2010**, *465*, 901−904.

(2) Klingler, S.; Pirro, P.; Brächer, T.; Leven, B.; Hillebrands, B.; Chumak, A. V. Design of a spin-wave majority gate employing mode selection. *Appl. Phys. Lett.* **2014**, *105*, 152410.

(3) Wagner, K.; Kákay, A.; Schultheiss, K.; Henschke, A.; Sebastian, T.; Schultheiss, H. Magnetic domain walls as reconfigurable spin-wave nanochannels. *Nat. Nanotechnol.* **2016**, *11*, 432−436.

(4) Trunk, T.; Redjdal, M.; Kákay, A.; Ruane, M. F.; Humphrey, F. B. Domain wall structure in Permalloy films with decreasing thickness at the Bloch to Néel transition. *J. Appl. Phys.* **2001**, *89*, 7606−7608.

(5) Allenspach, R.; Stampanoni, M.; Bischof, A. Magnetic domains in thin epitaxial Co/Au(111) films. *Phys. Rev. Lett.* **1990**, *65*, 3344−3347.

(6) O'Brien, L.; Petit, D.; Zeng, H. T.; Lewis, E. R.; Sampaio, J.; Jausovec, A. V.; Read, D. E.; Cowburn, R. P. Near-Field Interaction between Domain Walls in Adjacent Permalloy Nanowires. *Phys. Rev. Lett.* **2009**, *103*, 077206.

(7) Ruotolo, A.; Cros, V.; Georges, B.; Dussaux, A.; Grollier, J.; Deranlot, C.; Guillemet, R.; Bouzehouane, K.; Fusil, S.; Fert, A. Phase-locking of magnetic vortices mediated by antivortices. *Nat. Nanotechnol.* **2009**, *4*, 528−532.

(8) Freeman, M. R.; Choi, B. C. Advances in Magnetic Microscopy. *Science* **2001**, *294*, 1484−1488.

(9) Hiebert, W. K.; Stankiewicz, A.; Freeman, M. R. Direct Observation of Magnetic Relaxation in a Small Permalloy Disk by Time-Resolved Scanning Kerr Microscopy. *Phys. Rev. Lett.* **1997**, *79*, 1134−1137.

(10) Onose, Y.; Okamura, Y.; Seki, S.; Ishiwata, S.; Tokura, Y. Observation of Magnetic Excitations of Skyrmion Crystal in a Helimagnetic Insulator Cu$_2$OSeO$_3$. *Phys. Rev. Lett.* **2012**, *109*, 037603.

(11) Acremann, Y.; Strachan, J. P.; Chembrolu, V.; Andrews, S. D.; Tyliszczak, T.; Katine, J. A.; Carey, M. J.; Clemens, B. M.; Siegmann, H. C.; Stöhr, J. Time-Resolved Imaging of Spin Transfer Switching: Beyond the Macrospin Concept. *Phys. Rev. Lett.* **2006**, *96*, 217202.

(12) Awad, A. A.; Dürrenfeld, P.; Houshang, A.; Dvornik, M.; Iacocca, E.; Dumas, R. K.; Åkerman, J. Long-range mutual synchronization of spin Hall nano-oscillators. *Nat. Phys.* **2017**, *13*, 292−299.

(13) Acremann, Y.; Chembrolu, V.; Strachan, J. P.; Tyliszczak, T.; Stöhr, J. Software defined photon counting system for time resolved x-ray experiments. *Rev. Sci. Instrum.* **2007**, *78*, 014702.

(14) Feist, A.; Bach, N.; Rubiano da Silva, N.; Danz, T.; Möller, M.; Priebe, K. E.; Domröse, T.; Gatzmann, J. G.; Rost, S.; Schauss, J.; Strauch, S.; Bormann, R.; Sivis, M.; Schäfer, S.; Ropers, C. Ultrafast transmission electron microscopy using a laser-driven field emitter: Femtosecond resolution with a high coherence electron beam. *Ultramicroscopy* **2017**, *176*, 63−73.

(15) Rubiano da Silva, N.; Möller, M.; Feist, A.; Ulrichs, H.; Ropers, C.; Schäfer, S. Nanoscale Mapping of Ultrafast Magnetization Dynamics with Femtosecond Lorentz Microscopy. *Phys. Rev. X* **2018**, *8*, 031052.

(16) Bartell, J. M.; Ngai, D. H.; Leng, Z.; Fuchs, G. D. Towards a table-top microscope for nanoscale magnetic imaging using picosecond thermal gradients. *Nat. Commun.* **2015**, *6*, 8460.

(17) Bartell, J. M.; Jermain, C. L.; Aradhya, S. V.; Brangham, J. T.; Yang, F.; Ralph, D. C.; Fuchs, G. D. Imaging Magnetization Structure and Dynamics in Ultrathin Y$_3$Fe$_5$O$_{12}$/Pt Bilayers with High Sensitivity Using the Time-Resolved Longitudinal Spin Seebeck Effect. *Phys. Rev. Appl.* **2017**, *7*, 044004.

(18) Guo, F.; Bartell, J. M.; Ngai, D. H.; Fuchs, G. D. Phase-Sensitive Imaging of Ferromagnetic Resonance Using Ultrafast Heat Pulses. *Phys. Rev. Appl.* **2015**, *4*, 044004.

(19) Gray, I.; Moriyama, T.; Sivadas, N.; Stiehl, G. M.; Heron, J. T.; Need, R.; Kirby, B. J.; Low, D. H.; Nowack, K. C.; Schlom, D. G.; Ralph, D. C.; Ono, T.; Fuchs, G. D. Spin Seebeck Imaging of Spin-Torque Switching in Antiferromagnetic Pt/NiO Heterostructures. *Phys. Rev. X* **2019**, *9*, 041016.

(20) Gray, I.; Stiehl, G. M.; Heron, J. T.; Mei, A. B.; Schlom, D. G.; Ramesh, R.; Ralph, D. C.; Fuchs, G. D. Imaging uncompensated moments and exchange-biased emergent ferromagnetism in FeRh thin films. *Phys. Rev. Materials* **2019**, *3*, 124407.

(21) Mei, A. B.; Gray, I.; Tang, Y.; Schubert, J.; Werder, D.; Bartell, J.; Ralph, D. C.; Fuchs, G. D.; Schlom, D. G. Local Photothermal Control of Phase Transitions for On-Demand Room-Temperature Rewritable Magnetic Patterning. *Adv. Mater.* **2020**, *32*, 2001080.

(22) Janda, T.; et al. Magneto-Seebeck microscopy of domain switching in collinear antiferromagnet CuMnAs. *Phys. Rev. Materials* **2020**, *4*, 094413.

(23) Pfitzner, E.; Hu, X.; Schumacher, H. W.; Hoehl, A.; Venkateshvaran, D.; Cubukcu, M.; Liao, J.-W.; Auffret, S.; Heberle, J.; Wunderlich, J.; Kästner, B. Near-field magneto-caloritronic nanoscopy on ferromagnetic nanostructures. *AIP Adv.* **2018**, *8*, 125329.

(24) Karsch, J. C.; Bartell, J. M.; Fuchs, G. D. Near-field coupling of gold plasmonic antennas for sub-100 nm magneto-thermal microscopy. *APL Photonics* **2017**, *2*, 086103.

(25) Weiler, M.; Althammer, M.; Czeschka, F. D.; Huebl, H.; Wagner, M. S.; Opel, M.; Imort, I.-M.; Reiss, G.; Thomas, A.; Gross, R.; Goennenwein, S. T. B. Local Charge and Spin Currents in Magnetothermal Landscapes. *Phys. Rev. Lett.* **2012**, *108*, 106602.

(26) von Bieren, A.; Brandl, F.; Grundler, D.; Ansermet, J.-P. Space- and time-resolved Seebeck and Nernst voltages in laser-heated permalloy/gold microstructures. *Appl. Phys. Lett.* **2013**, *102*, 052408.

(27) Iguchi, R.; Kasai, S.; Koshikawa, K.; Chinone, N.; Suzuki, S.; Uchida, K.-I. Thermoelectric microscopy of magnetic skyrmions. *Sci. Rep.* **2019**, *9*, 18443.

(28) Seki, T.; Iguchi, R.; Takanashi, K.; Uchida, K. Relationship between anomalous Ettingshausen effect and anomalous Nernst effect in an FePt thin film. *J. Phys. D: Appl. Phys.* **2018**, *51*, 254001.

(29) Chuang, T. C.; Su, P. L.; Wu, P. H.; Huang, S. Y. Enhancement of the anomalous Nernst effect in ferromagnetic thin films. *Phys. Rev. B: Condens. Matter Mater. Phys.* **2017**, *96*, 174406.

(30) Pu, Y.; Chiba, D.; Matsukura, F.; Ohno, H.; Shi, J. Mott Relation for Anomalous Hall and Nernst Effects in Ga$_{1-x}$Mn$_x$As Ferromagnetic Semiconductors. *Phys. Rev. Lett.* **2008**, *101*, 117208.

(31) Miyasato, T.; Abe, N.; Fujii, T.; Asamitsu, A.; Onoda, S.; Onose, Y.; Nagaosa, N.; Tokura, Y. Crossover Behavior of the Anomalous Hall Effect and Anomalous Nernst Effect in Itinerant Ferromagnets. *Phys. Rev. Lett.* **2007**, *99*, 086602.

(32) Sharma, H.; Wen, Z.; Takanashi, K.; Mizuguchi, M. Anomaly in anomalous Nernst effect at low temperature for C1$_b$-type NiMnSb half-Heusler alloy thin film. *Jpn. J. Appl. Phys.* **2019**, *58*, SBBI03.

(33) Bennet, R. K.; Hojem, A.; Zink, B. L. Temperature dependence of the anomalous Nernst coefficient for Ni$_{80}$Fe$_{20}$ determined with metallic nonlocal spin valves. *AIP Adv.* **2020**, *10*, 065127.

(34) Bennet, R. K.; Hojem, A.; Zink, B. L. Thermal gradients and anomalous Nernst effects in membrane-supported nonlocal spin valves. *Phys. Rev. B: Condens. Matter Mater. Phys.* **2019**, *100*, 104404.

(35) Gautam, P.; Sharma, P. R.; Kim, Y.; Kim, T.; Noh, H. Temperature dependent anomalous Hall effect and anomalous Nernst effect in perpendicularly magnetized [CoSiB/Pt] multilayer film. *J. Magn. Magn. Mater.* **2018**, *446*, 264−269.

(36) Slachter, A.; Bakker, F. L.; van Wees, B. J. Anomalous Nernst and anisotropic magnetoresistive heating in a lateral spin valve. *Phys. Rev. B: Condens. Matter Mater. Phys.* **2011**, *84*, 020412.

(37) Hu, S.; Kimura, T. Anomalous Nernst-Ettingshausen effect in nonlocal spin valve measurement under high-bias current injection. *Phys. Rev. B: Condens. Matter Mater. Phys.* **2013**, *87*, 014424.

(38) Wegrowe, J.-E.; Drouhin, H.-J.; Lacour, D. Anisotropic magnetothermal transport and spin Seebeck effect. *Phys. Rev. B: Condens. Matter Mater. Phys.* **2014**, *89*, 094409.

(39) Meng, L.; Huang, T.; Wang, X.; Chen, S.; Yang, Z.; Ren, B. Gold-coated AFM tips for tip-enhanced Raman spectroscopy: theoretical calculation and experimental demonstration. *Opt. Express* **2015**, *23*, 13804−13813.

(40) Knoll, B.; Keilmann, F. Enhanced dielectric contrast in scattering-type scanning near-field optical microscopy. *Opt. Commun.* **2000**, *182*, 321−328.

(41) Roth, R. M.; Panoiu, N. C.; Adams, M. M.; Osgood, R. M.; Neacsu, C. C.; Raschke, M. B. Resonant-plasmon field enhancement from asymmetrically illuminated conical metallic-probe tips. *Opt. Express* **2006**, *14*, 2921−2931.

(42) Berweger, S.; Atkin, J. M.; Olmon, R. L.; Raschke, M. B. Adiabatic Tip-Plasmon Focusing for Nano-Raman Spectroscopy. *J. Phys. Chem. Lett.* **2010**, *1*, 3427−3432.

(43) Challener, W. A.; Peng, C.; Itagi, A. V.; Karns, D.; Peng, W.; Peng, Y.; Yang, X.; Zhu, X.; Gokemeijer, N. J.; Hsia, Y.-T.; Ju, G.; Rottmayer, R. E.; Seigler, M. A.; Gage, E. C. Heat-assisted magnetic recording by a near-field transducer with efficient optical energy transfer. *Nat. Photonics* **2009**, *3*, 220−224.

(44) Kryder, M. H.; Gage, E. C.; McDaniel, T. W.; Challener, W. A.; Rottmayer, R. E.; Ju, G.; Hsia, Y.-T.; Erden, M. F. Heat Assisted Magnetic Recording. *Proc. IEEE* **2008**, *96*, 1810−1835.

(45) Rausch, T.; Trantham, J. D.; Chu, A. S.; Dakroub, H.; Riddering, J. W.; Henry, C. P.; Kiely, J. D.; Gage, E. C.; Dykes, J. W. HAMR Drive Performance and Integration Challenges. *IEEE Trans. Magn.* **2013**, *49*, 730−733.

(46) Wu, A. Q.; et al. HAMR Areal Density Demonstration of 1+ Tbpsi on Spinstand. *IEEE Trans. Magn.* **2013**, *49*, 779−782.

(47) Zhang, Z.; Ahn, P.; Dong, B.; Balogun, O.; Sun, C. Quantitative Imaging of Rapidly Decaying Evanescent Fields Using Plasmonic Near-Field Scanning Optical Microscopy. *Sci. Rep.* **2013**, *3*, 2803.

(48) Wang, L.; Xu, X. G. Scattering-type scanning near-field optical microscopy with reconstruction of vertical interaction. *Nat. Commun.* **2015**, *6*, 8973.

(49) Conca, A.; Greser, J.; Sebastian, T.; Klingler, S.; Obry, B.; Leven, B.; Hillebrands, B. Low spin-wave damping in amorphous $Co_{40}Fe_{40}B_{20}$ thin films. *J. Appl. Phys.* **2013**, *113*, 213909.

(50) Liu, X.; Zhang, W.; Carter, M. J.; Xiao, G. Ferromagnetic resonance and damping properties of CoFeB thin films as free layers in MgO-based magnetic tunnel junctions. *J. Appl. Phys.* **2011**, *110*, 033910.

(51) Chen, S.; Tang, M.; Zhang, Z.; Ma, B.; Lou, S. T.; Jin, Q. Y. Interfacial effect on the ferromagnetic damping of CoFeB thin films with different under-layers. *Appl. Phys. Lett.* **2013**, *103*, 032402.

(52) Guo, F.; Bartell, J. M.; Fuchs, G. D. Ferromagnetic resonance phase imaging in spin Hall multilayers. *Phys. Rev. B: Condens. Matter Mater. Phys.* **2016**, *93*, 144415.

(53) Betzig, E.; Trautman, J. K.; Wolfe, R.; Gyorgy, E. M.; Finn, P. L.; Kryder, M. H.; Chang, C.-H. Near-field magneto-optics and high density data storage. *Appl. Phys. Lett.* **1992**, *61*, 142−144.

(54) Keatley, P. S.; Loughran, T. H. J.; Hendry, E.; Barnes, W. L.; Hicken, R. J.; Childress, J. R.; Katine, J. A. A platform for time-resolved scanning Kerr microscopy in the near-field. *Rev. Sci. Instrum.* **2017**, *88*, 123708.

(55) Reichlova, H.; Janda, T.; Godinho, J.; Markou, A.; Kriegner, D.; Schlitz, R.; Zelezny, J.; Soban, Z.; Bejarano, M.; Schultheiss, H.; Nemec, P.; Jungwirth, T.; Felser, C.; Wunderlich, J.; Goennenwein, S. T. B. Imaging and writing magnetic domains in the non-collinear antiferromagnet Mn_3Sn. *Nat. Commun.* **2019**, *10*, 5459.

(56) Neacsu, C. C.; Berweger, S.; Olmon, R. L.; Saraf, L. V.; Ropers, C.; Raschke, M. B. Near-Field Localization in Plasmonic Super-focusing: A Nanoemitter on a Tip. *Nano Lett.* **2010**, *10*, 592−596.

(57) Ropers, C.; Neacsu, C. C.; Raschke, M. B.; Albrecht, M.; Lienau, C.; Elsaesser, T. Light Confinement at Ultrasharp Metallic Tips. *Jpn. J. Appl. Phys.* **2008**, *47*, 6051−6054.

(58) Berweger, S.; Atkin, J. M.; Olmon, R. L.; Raschke, M. B. Light on the Tip of a Needle: Plasmonic Nanofocusing for Spectroscopy on the Nanoscale. *J. Phys. Chem. Lett.* **2012**, *3*, 945−952.

(59) Ropers, C.; Neacsu, C. C.; Elsaesser, T.; Albrecht, M.; Raschke, M. B.; Lienau, C. Grating-Coupling of Surface Plasmons onto Metallic Tips: A Nanoconfined Light Source. *Nano Lett.* **2007**, *7*, 2784−2788.

https://doi.org/10.1021/acs.nanolett.1c00704
Nano Lett. 2021, 21, 4966−4972